Online Research @ Cardiff

information services
gwasanaethau gwybodaeth

Ice Mass Change in Greenland and Antarctica between 1993 and 2013 from Satellite Gravity Measurements

Matthieu J. Talpe · R. Steven Nerem · Ehsan Forootan · Michael Schmidt · Frank G. Lemoine · Ellyn M. Enderlin · Felix W. Landerer

Abstract We construct long-term time series of Greenland and Antarctic ice sheet mass change from satellite gravity measurements. A statistical reconstruction approach is developed based on a Principal Component Analysis to combine high-resolution spatial modes from the Gravity Recovery and Climate Experiment (GRACE) mission with the gravity information from conventional satellite track-

M. Talpe · R. S. Nerem
Aerospace Engineering Sciences, University of Colorado Boulder
429 UCB University of Colorado Boulder
Boulder, CO, 80309, USA
E-mail: matthieu.talpe@colorado.edu
E-mail: nerem@colorado.edu

E. Forootan
School of Earth and Ocean Sciences, Cardiff University
Park Pl
CF10 3AT, Cardiff, United Kingdom
E-mail: ForootanE@cardiff.ac.uk

M. Schmidt
Deutsches Geodätisches Forschungsinstitut (DGFI), Technische Universität München
Alfons-Goppel-Straße 11
80539 München, Germany
E-mail: mg.schmidt@tum.de

F. G. Lemoine
Planetary Geodynamics Laboratory, NASA Goddard Space Flight Center
Greenbelt, MD 20771, USA
E-mail: frank.g.lemoine@nasa.gov

E. M. Enderlin
Climate Change Institute, University of Maine
300E Bryand Global Sciences Center
Orono, ME 04469-5790, USA
E-mail: ellyn.enderlin@maine.edu

F. W. Landerer
Jet Propulsion Laboratory, California Institute of Technology
4800 Oak Grove Dr.
Pasadena, CA 91109, USA
E-mail: felix.w.landerer@jpl.nasa.gov

ing data. Uncertainties of this reconstruction are rigorously assessed; they include temporal limitations for short GRACE measurements, spatial limitations for the low-resolution conventional tracking data measurements, and limitations of the estimated statistical relationships between low and high degree potential coefficients reflected in the PCA modes. Trends of mass variations in Greenland and Antarctica are assessed against a number of previous studies. The resulting time series for Greenland show a higher rate of mass loss than other methods before 2000, while the Antarctic ice sheet appears heavily influenced by interannual variations.

Keywords time-variable Gravity · Mass Change · Greenland · Antarctica

1 Introduction

Efforts to assess the mass balance of the Greenland and Antarctic ice sheets hinge on a number of different satellite-based data types (InSAR, radar altimetry, gravimetry, etc.) and regional models (surface mass balance, atmospheric pressure, etc.), some with longer time series than others (*Rignot et al.*, 2011; *Shepherd et al.*, 2012; *Velicogna and Wahr*, 2013). One way of monitoring these mass change variations is from satellite-based, time-variable gravity estimates (*Wahr et al.*, 1998). Since April 2002, the Gravity Recovery and Climate Experiment (GRACE) mission has used high-precision K-band microwave ranging to deliver estimates of time-variable gravity on a monthly basis and with spatial resolution equivalent to a disk of radius 330 km (*Tapley et al.*, 2004). However, the short span of the GRACE-derived time series (less than two decades) places limitations on the interpretation of scientific products and on the proper detection and isolation of trends and interannual gravity variations. This study seeks to extend the record of Greenland and Antarctic mass change observed by GRACE by merging them with complementary time-variable gravity information that spans back to November 1992, thereby adding a full decade of perspective prior to the GRACE time frame. Complementary time-variable gravity information comes from the conventional tracking of a suite of satellites via Satellite Laser Ranging (SLR) and Doppler Orbitography and Radiopositioning Integrated by Satellites (DORIS).

A number of studies have already investigated the use of SLR products as a basis to detect and interpret time-variable gravity signals. *Cox and Chao* (2002), *Nerem and Wahr* (2011), and *Cheng et al.* (2013) have shown that time series of J_2 estimates, where J_2 is the zonal coefficient describing the oblateness of the Earth, provide a reliable metric to measure the combined contribution of the Greenland and Antarctic ice sheet balance. *Morrow et al.* (2013) argue, however, that the next even zonal coefficient J_4 provides a metric of even higher reliability because of smaller contamination from other signals, such as the Glacial Isostatic Adjustment (GIA), the 18.6-year solid Earth body tide, and core-mantle coupling. Zonal harmonics can also be used as observations and/or constraints to invert for various geodetic parameters: *James and Ivins* (1997) show that polar mass balance estimates are highly sensitive to odd-degree zonal harmonic, while *Tosi et al.* (2005) find that the Greenland and Antarctic ice sheets lose 280 and 60 Gt/yr of ice mass, respectively, using 26 years of secular variations in SLR-derived zonal harmonics (presumably starting soon after the launch of LAGEOS-1). *Matsuo et al.* (2013) employ an SLR-based field of degree and order four to show that SLR tracking

provides a consistent benchmark to assess the history of mass variations in Greenland. Similarly, *Cerri et al.* (2013) estimated Greenland mass change solely from DORIS-based tracking solutions. The high-low, satellite-to-satellite, GPS-based tracking data of the Challenging Minisatellite Payload (CHAMP) satellite have been used to extract trends and annual amplitude of mass change in Greenland over CHAMP's lifetime (2000-2010) (*Baur*, 2013; *Weigelt et al.*, 2013). Finally, the recently launched, three-satellite mission Swarm also holds much promise for time-variable gravity studies, as well as other high-low GPS-based approaches (*Sośnica et al.*, 2015; *Zehentner and Mayer-Gürr*, 2015).

In contrast to the studies described above that use uniquely the conventional tracking data, this study seeks to combine SLR and DORIS with GRACE time-variable products. Indeed, the GRACE fields are high spatial resolution but cover a relatively shorter timespan (April 2002 onward) while the SLR/DORIS fields are low spatial resolution but cover a longer timespan (November 1992 onward). By combining these datasets into a single and distinct set of monthly fields, our analysis seeks to overcome their respective shortcomings and extends the time-variable gravity information by a full decade prior to the GRACE period, placing the changes observed by GRACE since April 2002 into a longer-term context. As such, the resulting gravity fields, obtained from the combination of GRACE and SLR/DORIS measurements, provide the first perspective of ice sheet mass change starting in the early 1990s from satellite gravimetry at a resolution higher than degree four. While other studies sought to combine the two types of fields at the normal equation level (e.g., *Haberkorn et al.* (2015)) and only low degree and order coefficients, this study combines the final products including all available Stokes coefficients.

In Section 2, the data and processing strategies are discussed. The reconstruction method for combining the fields is presented in Section 3. In Section 4, the resulting mass change curves and their associated errors are described, while in Section 5 we discuss the validity of the mass change curves during the GRACE interval and before using comparisons against GRACE-only solutions and another independent estimate for Greenland, respectively.

2 Data

There are two types of satellite gravity solutions used in our analysis (Table 1). The first type originates from the latest processing (RL05) of GRACE data from the Center for Space Research (CSR) at UT-Austin (*Bettadpur*, 2012). These gravity products are monthly fields up to degree and order 60. The second type is from a suite of satellites tracked via SLR and DORIS, where observations are accumulated into weekly normal equations used to solve for 33 Stokes coefficients and their associated full covariances at Goddard Space Flight Center (GSFC) (*Lemoine et al.*, 2014).

The GSM component of the GRACE data is used without adding any of the background models from AOD1B (*Flechtner et al.*, 2015; *Dobslaw et al.*, 2013). The remaining differences in background models between SLR/DORIS and the GRACE fields are not treated in this study. We believe that their influences are smaller than other sources of errors introduced by the method described in Section 3.

While low-resolution SLR solutions are available starting in 1976 with the launch of LAGEOS-1, the SLR/DORIS solutions used in this study (*Lemoine et al.*, 2014) start in November 1992 because only then can full solutions larger than degree two be estimated. In addition, the focus of this particular SLR/DORIS solution was to develop a time-variable gravity time series that could be used to improve the orbits of altimetry satellites (*Lemoine et al.*, 2010) and to contribute reprocessed data to the realization of ITRF2014 (*Lemoine et al.*, 2016). Expanding the spherical harmonic time series backwards would require a new processing strategy to accommodate for a different, time-evolving satellite constellation and challenges in the SLR data quality. Finally, the weekly SLR/DORIS solutions and associated covariances are averaged to monthly solutions to match the GRACE monthly time steps.

For this analysis, the GRACE and SLR/DORIS gravity fields are processed almost similarly. But first, specific corrections are applied to GRACE fields: destriping (*Swenson and Wahr*, 2006), Gaussian smoothing with 300 km radius (*Jekeli*, 1981), C_{21} and S_{21} trend corrections (*Wahr et al.*, 2015), and C_{20} value replacement (*Cheng et al.*, 2011). For both fields, we then remove the influence of Glacial Isostatic Adjustment (GIA) via the ICE-6G_C (VM5a) model (*Peltier et al.*, 2015), the mean of the fields over the GRACE timespan, and the annual and semi-annual components of seasonal signals. We choose to remove the seasonal signals because we are interested in interannual signals. Furthermore, the degree-one coefficients in GRACE are neglected because degree-one coefficients were not estimated in the SLR/DORIS fields. While the point of the study is to resolve higher degree and order coefficients prior to the GRACE period using SLR/DORIS, we believe that resolving the longest wavelength coefficients (i.e., degree-one) is not adapted to the technique presented here.

A comparison of the GRACE and SLR/DORIS coefficients indicates good agreement, especially for degree two coefficients, C_{30}, and the sectorals (*Lemoine et al.*, 2016). Correlations between GRACE and SLR/DORIS coefficients are illustrated in Figure 2 of the Supplemental Information in *Lemoine et al.* (2014).

3 Method

Combining gravity fields from GRACE and SLR/DORIS relies on one fundamental step: the projection of global gravity field modes onto SLR/DORIS fields (Section 3.1). A notable feature of the proposed approach is that the PCA is applied to GRACE fields in the spectral domain (Section 3.2). The projection of these global gravity modes onto SLR/DORIS fields is estimated via a Least Squares Adjustment (LSA) (Section 3.3), in which incorporating the information from the SLR/DORIS covariances is necessary given the existing correlations between Stokes coefficients. The solution of this LSA is a set of temporal amplitudes associated with each global gravity mode. Finally, the number of modes N_{modes} used for combining GRACE and SLR/DORIS products is justified in Section 3.4 (although the determination of this number is not a critical step). All in all, the reconstructed fields are computed by summing the combination of the N_{modes} global gravity modes with their temporal amplitude.

3.1 Overview of the PCA Reconstruction

In this section, we provide an overview of the Principal Component Analysis (PCA) method and its relation to the reconstruction process. Though a detailed description of PCA and its application for analyzing time-variable gravity products is provided in *Forootan* (2014) and *Preisendorfer* (1988), we provide the main equations to better understand the reconstruction algorithm.

The global time-variable gravity products used here (SLR/DORIS and GRACE) show mass redistribution concentrated mostly over land. Each component possesses its own set of subcomponents that operate at different spatial and temporal scales. The PCA approach is applied here to extract orthogonal (uncorrelated) spatial and temporal patterns that capture the dominant variability in the GRACE fields.

The first step of a PCA is to build a data matrix $\mathbf{X}$ consisting of monthly time series $\mathbf{x}_i$, where i represents the time index ($i = 1, ..., N_{months}$) of the global fields. In this study, the time series $\mathbf{x}_i$ are column vectors each comprised of N_{coeffs} temporally centered Stokes coefficients (i.e., the mean is removed from each row of $\mathbf{X}$).

Then, an auto-covariance matrix $\mathbf{C}$ is built from $\mathbf{X}$ ($\mathbf{C} = \mathbf{X}^T\mathbf{X}/N_{months}$) and decomposed into its eigenvector basis $\mathbf{H}_0$ of size $N_{coeffs} \times N_{months}$. $\mathbf{H}$ represents a reduced version of $\mathbf{H}_0$ and only contains the first N_{modes} dominant modes, where N_{modes} is defined in Section 3.4. $\mathbf{H}$ therefore has a size $N_{coeffs} \times N_{modes}$. Columns of this matrix $\mathbf{H}$ are the eigenvectors $\mathbf{h}_k$ ($k = 1, ..., N_{modes}$) of length N_{coeffs}. They are also known as the Empirical Orthogonal Functions (EOFs) and contain the spatial information of the multi-dimensional data matrix $\mathbf{X}$.

To determine the temporal evolution of each EOF $\mathbf{h}_k$, $\mathbf{H}$ is projected onto the data matrix $\mathbf{X}$ (i.e., $\mathbf{Y} = \mathbf{H}^T\mathbf{X}$). The matrix $\mathbf{Y}$ contains the Principal Components (PCs) of size $N_{modes} \times N_{months}$, where the N_{months} entries of each row represent a PC $\mathbf{y}_k$ that is uniquely associated with an EOF by describing its temporal behavior. In other words, over each epoch i, an EOF $\mathbf{h}_k$ is scaled by $\mathbf{y}_k(t_i)$.

An approximation of the original multi-dimensional data $\mathbf{Z}_{Rec}$ is reconstructed from a linear combination of each mode's EOF and its respective PC: $\mathbf{Z}_{Rec} = \mathbf{HY} = \sum_{k=1}^{N_{modes}} \mathbf{h}_k\mathbf{y}_k$. The reconstructed data matrix $\mathbf{Z}_{Rec}$ is a set of time series of Stokes coefficients of size $N_{coeffs} \times N_{months}$.

The key of the study is the fact that the EOFs $\mathbf{H}$ come from GRACE and the PCs $\mathbf{Y}$ from the SLR/DORIS fields. Hence, the reconstruction entails that information from GRACE, which contains spatial information of high resolution, is combined with temporal information from SLR/DORIS, which offers an additional decade of coverage compared to GRACE.

Analogous reconstruction techniques (i.e., combining two datasets, each with its distinct temporal or spatial resolution advantage) have been applied in sea-level reconstructions, whereby high-resolution and global spatial modes obtained from satellite altimetry are combined with decades of relatively spatially inhomogeneous times series from tide gauges (*Kaplan et al.*, 2000; *Church and White*, 2002; *Hamlington et al.*, 2011; *Ray and Douglas*, 2011).

3.2 Data Matrix and EOFs of Stokes Coefficients

To combine SLR and GRACE products, we apply PCA to a data matrix of monthly time series of Stokes coefficients. The use of Stokes coefficients as data contrasts with applying a PCA on a data matrix of grid cells. This choice is motivated by the inability to calculate full-rank covariances matrices in the grid cell approach. Full-rank matrices are necessary in order to compute the temporal modes, as outlined in Section 3.3.

There are $N_{coeffs}^{SD} = 33$ coefficients per epoch in SLR/DORIS fields, as opposed to $N_{coeffs}^{G} = 3627$ coefficients for GRACE fields. Each covariance matrix $\mathbf{P}_{stokes}^{j}$ ($j = 1, ..., N_{months}^{SD}$) and its inverse, the weighting matrix $\mathbf{W}_{stokes}^{j}$, are therefore a square matrix of of size 33×33. Mapping Stokes coefficients to a grid of Equivalent Water Thickness (EWT) is straightforward as outlined in *Wahr et al.* (1998),' but mapping the weighting matrices of Stokes coefficients from the SLR/DORIS field to the grid space (as required in Section 3.3) is hindered by singular matrices.

An EWT gridded field at an epoch i is computed as follows:

$$EWT(\theta_1, \phi_1, t_i) = \frac{a\rho_e}{3\rho_w} \sum_{l=0}^{\infty} \sum_{m=0}^{l} \left(\frac{2l+1}{k_l+1}\right) \tilde{P}_{lm}(\cos(\theta_1))(\Delta C_{lm}(t_i)\cos(m\phi_1) + \Delta S_{lm}(t_i)\sin(m\phi_1))$$

$$\mathbf{EWT}(t_i) = [EWT(\theta_1, \phi_1, t_i), EWT(\theta_2, \phi_2, t_i), ..., EWT(\theta_{N_{pix}}, \phi_{N_{pix}}, t_i)]$$

$$= \mathbf{Q}\mathbf{z}(t_i) \tag{1}$$

where a is the mean radius of the Earth, ρ_w the density of water, ρ_e the average density of the Earth, θ and ϕ the co-latitude and longitude, respectively, k_l the Love numbers of degree l, and $\tilde{P}_{lm}$ the normalized associated Legendre functions (*Wahr et al.*, 1998). The matrix $\mathbf{EWT}$ contains all spatio-temporal EWT information. The column vector $\mathbf{z}(t_i)$ contains N_{coeffs}^{SD} Stokes coefficients of a monthly SLR/DORIS field and the matrix $\mathbf{Q}$ is the mapping function from spectral domain to grid space. The matrix $\mathbf{Q}$ has a size $N_{pix} \times N_{coeffs}^{SD}$, where N_{pix} is the desired numbers of pixels in the grid. A grid with 5 degree/pixel would translate to 2592 pixels (36×72) and, therefore, a size for $\mathbf{Q}$ of $2592 \times N_{coeffs}^{SD}$.

By standard error propagation, the covariance matrix $\mathbf{P}_{stokes}$ can be converted to EWT grid space as $\mathbf{P}_{grid} = \mathbf{Q}\mathbf{P}_{stokes}\mathbf{Q}^{T}$. The equivalent weighting matrix $\mathbf{W}_{grid}$ is simply the inverse of $\mathbf{P}_{grid}$. But considering the fact that $\mathbf{P}_{stokes}$ has a rank of N_{coeffs}^{SD}, the propagated $\mathbf{P}_{grid}$ is a square matrix of size N_{pix}, which for $N_{pix} >> N_{coeffs}^{SD}$, is rank-deficient. Two common methods to mitigate this issue of rank-deficiency include reducing the dimensionality of $\mathbf{P}_{stokes}$ and adding a priori information. Reducing the matrix's dimensionality to match the rank of the input data translates to $N_{pix} \leq N_{coeffs}^{SD} = 33$, i.e., a map with 33 pixels. The resolution of such a map is not only unacceptably small for the purposes of this study, but its equivalent $\mathbf{P}_{stokes}$ also still possesses a high condition number (10^{17}) (*Koch*, 1988). Regarding the second method, there is currently no known way to estimate a priori information for covariances of global gravity field coefficients starting in 1992.

The limitations that arise from estimating SLR/DORIS weighting matrices force us to keep the data and covariances in Stokes space, in which the reconstruction can be applied more consistently. When applying PCA, the columns of data matrix $\mathbf{X}$ should represent a comparable quantity. For instance to apply

PCA in the grid domain, *Forootan and Kusche* (2012) suggest to weight $\mathbf{X}$ by a latitude-dependent cosine function to account for the differences in grid area. In the spectral domain, we assign a degree-dependent weighting function because lower degree coefficients should have a larger contribution to the data matrix.

In summary, building the data matrix $\mathbf{X}$ involves two specific steps particular to this study. First, limitations in computing SLR/DORIS weighting matrix (necessary for later steps) forces us to construct the data matrix $\mathbf{X}$ using Stokes coefficients. Second, the Stokes coefficients are weighted according to their wavelength to normalize the contribution of each coefficient to the data matrix $\mathbf{X}$. Finally, we use this data matrix of Stokes coefficients $\mathbf{X}$ in a regular PCA decomposition. This inherently yields an EOF matrix $\mathbf{H}$ composed of Stokes coefficients.

3.3 Least Squares Adjustment (LSA) of PCs

Generally speaking, we assume that we can estimate the SLR/DORIS-derived PCs (as opposed to the PCs from the GRACE PCA) by projecting the EOFs from GRACE onto each SLR/DORIS monthly field via a LSA. The advantage of this projection is that the EOFs are basis functions that represent the physical characteristics of the gravity fields from GRACE. This contrasts with projecting customized spatial patterns onto SLR/DORIS fields, such as distinct fingerprints of continental basins. In that case, one would be forcing basis functions without any direct connection to the physical reality seen by GRACE.

The matrix $\mathbf{Y}_{SD}$ contains this temporal information (the PCs) from SLR/DORIS observations. Each column y_{SD}^{j} represents the principal components of all modes at a specific month j. The vector $\mathbf{y}_{SD}^{j}$ is estimated from a LSA of the truncated GRACE spatial modes $\mathbf{H}_{G}^{trunc}$ (size $N_{coeffs}^{SD} \times N_{modes}$) onto a monthly set of SLR/DORIS coefficients $\mathbf{x}_{SD}^{j}$ (size $N_{coeffs}^{SD} \times 1$) (see below for further clarification on the meaning of $\mathbf{H}_{G}^{trunc}$). The observation equation can be described as $\mathbf{x}_{SD}^{j} = \mathbf{H}_{G}^{trunc}\mathbf{y}_{SD}^{j}$ and its equivalent LSA in Eq. 2.

$$\mathbf{y}_{SD}^{j} = \left((\mathbf{H}_{G}^{trunc})^{T}\mathbf{W}_{SD}^{j}\mathbf{H}_{G}^{trunc}\right)^{-1}\left((\mathbf{H}_{G}^{trunc})^{T}\mathbf{W}_{SD}^{j}\mathbf{x}_{SD}^{j}\right) \qquad (2)$$

The weighting matrices are the inverses of the given SLR/DORIS covariances, $\mathbf{W}_{SD}^{j}$ (size $N_{coeffs}^{SD} \times N_{coeffs}^{SD}$). The reconstruction hinges on these weighting matrices because the SLR/DORIS Stokes coefficients are correlated. Without the covariances, the resulting temporal modes lead to reconstructed gravity fields that are drastically different.

The observation equation is an approximation of the PCA decomposition of the SLR/DORIS fields. Normally, we would have $\mathbf{X}_{SD} = \mathbf{H}_{SD}\mathbf{Y}_{SD}$. However, we replaced $\mathbf{H}_{SD}$ with $\mathbf{H}_{G}^{trunc}$. In other words, we have assumed that the cross-correlations between the gravity coefficients over 11/1992 – 04/2014 (the time frame of SLR/DORIS) are the same as those over 04/2002 – 06/2016 (the time frame of GRACE). In the statistical language, we consider that the EOF patterns are stationary over 11/1992 – 04/2014. The error of this assumption is estimated in Section 4.3.2.

It is worth mentioning that to estimate the temporal modes $\mathbf{Y}$, the original EOFs $\mathbf{H}_{G}$ are truncated to match the resolution of the SLR/DORIS fields, as illustrated in Figure 1. This truncation involves removing all Stokes coefficients of

degree and order that do not match that of the SLR/DORIS fields to find the associated temporal components (i.e., by reducing the size each $\mathbf{h}_k$ from $N_{coeffs}^G \times 1$ to $N_{coeffs}^{SD} \times 1$). The option of truncating a field provides an opportunity to easily switch between resolutions (e.g., 60x60 field becomes a 5x5 field by simply removing all unwanted Stokes coefficients, and then back to 60x60 by adding the Stokes coefficients back in) and therefore highlights another advantage of keeping the data in spectral domain (Stokes coefficients) instead of grids, with which it is much more complicated to switch resolutions. When truncating Stokes fields, one should note that the orthonormality of EOFs is violated, i.e., $\mathbf{h}_{k_1}^T \mathbf{h}_{k_2} = 0$, but $(\mathbf{h}_{k_1}^{trunc})^T \mathbf{h}_{k_2}^{trunc} \neq 0$. However, our numerical assessment indicates that the truncation from the original GRACE to the SLR/DORIS resolution does not significantly harm the orthogonality. Therefore, this is an acceptable step and would have no significant influence on the final reconstruction results.

The LSA yields a covariance term that contains the information on the errors and cross-correlations of the PCs $\mathbf{y}_{SD}$, $\mathbf{P}_y^j = ((\mathbf{H}_G^{trunc})^T \mathbf{W}_{SD}^j \mathbf{H}_G^{trunc})^{-1}$. The resulting correlations are mostly due to existing correlations in the SLR/DORIS covariances but also, to a lesser extent, from the fact that the columns of $\mathbf{H}_G^{trunc}$ are no longer orthogonal. However, the highest correlations remain under 0.5 and are statistically insignificant.

3.4 Number of Modes

The number of modes N_{modes} determines how many parameters are solved for in the LSA in Eq 2 at each epoch. Each parameter is the temporal amplitude associated with each EOF spatial mode (see Section 3.3). In regular PCA methods, the number modes can be selected from dominant-variance rules, sampling error rules such as North's rule of thumb (*North et al.*, 1982), etc. Many of these rules are summarized in *Forootan* (2014). We find that 22 modes, for example, suffice to explain 95% of the original variance in the GRACE fields.

However, in this study, we are limited by the ability of the model in the LSA to solve for parameters given the 33 observations per epoch. The model is the EOF matrix ($N_{obs} \times N_{modes}$) and the 33 observations are the SLR/DORIS coefficients. On one hand, when the number of modes solved for is too low (below three), this means that the total global reconstructed fields are only based on two modes. Therefore, independent regional variability is severely limited, which is an issue for this study because we would like signals in Greenland and Antarctica to be uncorrelated. On the other hand, when the number of modes is too high (above six), the comparison between reconstructed global maps and GRACE maps over similar time frames is clearly worst (i.e., the average RMS of the differences between the maps is higher). We balance the two extremes by setting $N_{modes} = 4$, although the differences between reconstructions using four through eight modes are not significant.

4 Results

4.1 Reconstruction Using Orthogonal Modes (EOFs & PCs)

The reconstructed global gravity fields $\mathbf{Z}_{rec}$ are obtained by combining the full GRACE spatial modes $\mathbf{H}_G$ ($\neq \mathbf{H}_G^{trunc}$) with the SLR/DORIS-based temporal modes: $\mathbf{Z}_{rec} = \mathbf{H}_G \mathbf{Y}_{SD}$. Figure 2 shows the modes.

The matrix $\mathbf{H}_G$ contains spatial information (the EOFs) derived solely from the PCA of the GRACE data matrix $\mathbf{X}$ (hence the "G" subscript). These EOFs reflect the spatial distribution of the geophysical processes that explain most of the variance in the global, time-variable, monthly fields obtained from GRACE between 04/2002 and 06/2016.

Each EOF $\mathbf{h}_k$ is comprised of Stokes coefficients that are evaluated into a global grid of EWT (see left column Figure 2). Mode 1 captures a secular trend mainly indicating the mass loss of the polar regions (e.g., *Forootan and Kusche* (2012)), which could be expected because the trend is the largest signal in time-variable gravity fields in which seasonal signals are removed. The three other modes reflect hydrologic signals, such as droughts in northeast Australia (mode 2), as well as residuals from seasonal effects (e.g., the Amazon basin) in several of the modes (*Rodell et al.*, 2004) and also residuals of stripes, especially observed over Antarctica. The EOFs obtained from a PCA on GRACE products from other processing centers (Jet Propulsion Laboratory (*Watkins and Yuan*, 2014) and GeoForschungsZentrum (*Dahle et al.*, 2013)) yield similar results: a trend mode capturing 65-70% of the variance followed by modes showing variability in land hydrology and residual non-tidal ocean, each capturing 2-8% of the variance. The PCs from GRACE are shown against the PCs from SLR/DORIS in Figure 2. There are inherent differences between the two sets, since the GRACE PCs represent a direct output of the PCA process, while the SLR/DORIS PCs are the solved parameters from an inversion of the truncated GRACE EOFs onto SLR/DORIS. As such, the SLR/DORIS PCs contain high-frequency artifacts that can be traced back to the variability in the SLR/DORIS covariances. Nonetheless, there is broad agreement between the two time series: for each mode, most long-wavelength behavior is recovered.

It is worth mentioning that in order to distribute the variance in a more balanced way, one might rotate the dominant EOFs to derive a new basis, e.g., the "varimax" criterion, which seeks to "maximize the contrast" between the regions containing the high variance via an optimal rotation (*Forootan and Kusche*, 2012). However, the first mode of various Rotated EOF sets still contained the combined signal from Greenland and Antarctica and still dominated the other modes.

The matrix $\mathbf{Y}_{SD}$ contains the temporal information (the SLR-DORIS-derived PCs from the LSA, blue curves in Figure 2) from SLR/DORIS observations projected onto the EOFs, as discussed in Section 3.3. In Figure 2, we also show the PCs from the GRACE-only decomposition (red curve) for comparison.

4.2 Computing Regional Mass Change Curves

Time series of cumulative mass change of the Greenland and Antarctic ice sheets are obtained by convolving a regional kernel with the reconstructed gravity fields,

as outlined in *Swenson and Wahr* (2002), and smoothed by applying a 12-month moving average. It is worth noting that this 12-month smoothing requires a 6-month truncation on both ends of the time series, so the resulting time series span 04/1993 – 11/2013 instead of 11/1992 – 04/2014. In the spatial domain, the regional kernels are global grids with a value of zero outside the region of interest and one within. In the case of Greenland and Antarctica, the contours are simply chosen as the coastlines plus 300 km, which ensures that the land signal is fully captured. This extra area introduces signal from the residual non-tidal ocean signal and is taken into account in the error budget in Section 4.3.4. The conversion of the kernel from the spatial domain to the spectral domain is set to a maximum degree of 60 in order to match the size of the gravity fields with which it is convolved. This necessary cutoff leads to an artificial smoothing of the kernel. This artificial smoothing of the kernel yields an artificial loss of mass that requires compensation via a scaling factor (*Velicogna and Wahr*, 2006). We estimate the scaling factor by calculating the ratio of the kernel area in the spatial domain to the kernel area in the spectral domain (see Eqs. 3 and 4 in *Longuevergne et al.* (2010)). For Greenland and Antarctica, the scale factors are 1.3 and 1.0, respectively.

4.3 Error Budget

The total error budget of each mass curve is composed of two broad types of errors: those from the reconstruction process of two different gravity fields and those inherent to satellite-derived, global gravity fields. The first broad type of error (from the reconstruction process, i.e., combining the GRACE EOFs with their associated temporal amplitudes from the LSA of SLR/DORIS fields onto GRACE modes) is further classified in three separate errors called the measurement error, the stationarity assumption error, and the truncation error. The second broad type of error is simply classified as an inherent geophysical error. In total, we treat the four errors in the following sections and illustrate their magnitude as a function of time in Figure 3. All errors described here are added in quadrature.

4.3.1 Measurement Error

The errors derived from the given SLR/DORIS full covariances represent the measurement error component of the total error budget (blue curve in Figure 3). First, the SLR/DORIS covariance at epoch j (size $N_{coeffs}^{SD} \times N_{coeffs}^{SD}$) is propagated to errors in the temporal components: $\mathbf{P}_{\mathbf{y}}^{j} = ((\mathbf{H}_{G}^{trunc})^{T} \mathbf{W}_{SD}^{j} \mathbf{H}_{G}^{trunc})^{-1}$ (see also Eq. 2). Second, the covariance matrix of the temporal modes $\mathbf{P}_{\mathbf{y}}^{j}$ (size $N_{modes} \times N_{modes}$) is propagated to errors in the reconstruction step, in which EOFs $\mathbf{H}_{G}$ from GRACE are combined with SLR/DORIS-derived PCs $\mathbf{Y}$, so that $\mathbf{P}_{field}^{j} = \mathbf{H}_{G} \mathbf{P}_{\mathbf{y}}^{j} \mathbf{H}_{G}^{T}$. The third and last step is the propagation of this covariance $\mathbf{P}_{field}^{j}$ into a covariance of mass change in the basin of interest, as described in Eq. (17) in *Swenson and Wahr* (2002). This step uses the reconstructed Stokes coefficients ΔC_{lm} and ΔS_{lm} to obtain the mass change in a region M^{j}. Because this operation is a linear combination of the reconstructed Stokes coefficients, it can be written in matrix form, i.e., $M^{j} = \mathbf{A}\mathbf{z}^{j}$, where $\mathbf{A}$ is a matrix containing the linear coefficients (size $1 \times N_{coeffs}^{G}$) and $\mathbf{z}^{j}$ a column vector of reconstructed

Stokes coefficients at epoch j (size $N_{coeffs} \times 1$). Hence, the covariance matrix of the mass calculation is now defined as $\mathbf{P}_M^j = \mathbf{A}\mathbf{P}_{field}^j\mathbf{A}^T$ (size 1×1). This value is the variance in the Greenland and Antarctic ice sheet mass reconstructions that originally came from the SLR/DORIS covariances.

The measurement error evolves in time because the accuracy of the SLR/DORIS fields is dependent on the number of satellites present in the solution and because of the changing quality of the tracking system and of its observations. A notable example is the tracking of Envisat (2002–2012), which strongly influences the solution by reducing the errors and correlations between the SLR/DORIS coefficients. This is due to its relatively low altitude, high inclination, and continuous orbit coverage (*Lemoine et al.*, 2016). The error associated with the Greenland mass change curve ranges between 60 and 140 Gt while the Antarctic error ranges between 30 and 50 Gt. The temporal behavior of this measurement error is similar for Greenland and Antarctica because they are both mostly defined by mode 1, as seen in Figure 2. This dependence on mode 1 is carried through the uncertain propagation steps outlined above. Finally, the larger magnitude of Greenland's error compared to Antarctica's is a consequence of its larger signal.

4.3.2 stationarity assumption Error

The assumption that the GRACE spatial modes $\mathbf{H}_G$ span the SLR/DORIS time frame yields an error that we call the "stationary" assumption error (yellow curve in Figure 3). Indeed, this assumption is inherently imperfect because the geophysical processes that dominated over the GRACE time frame are not exactly the same over the SLR/DORIS time frame. To estimate these errors, we simulate 30 unique and separate reconstructions, each using EOFs calculated from a PCA on limited GRACE data. Limited GRACE data means that the GRACE fields do not contain the full set of monthly fields, but rather have a unique pseudo-randomly generated gap. "Pseudo-randomly" entails that gaps of constrained lengths (between three and six years) and constrained midpoints (between 2006 and 2012) were, other than those two constraints, created randomly. This pseudo-randomness is justified because other more specific families of gaps (with either fixed length, or fixed midpoint, or both, etc.) yielded similar results. The use of simulated gaps seeks to recreate the lack of GRACE data over the SLR/DORIS time frame. For each simulated set of EOFs, we follow the method described in Section 3 and reconstruct 30 unique mass change curves for the Greenland and Antarctic ice sheets.

These 30 reconstructed mass change curves are then compared to the "truth" mass change curve from a reconstruction using the full GRACE data, denoted as gray lines and a blue line, respectively, in Figure 4. To quantify the errors, we examine the residuals (simulated minus truth), and their mean is plotted in purple in Figure 4 and in yellow in Figure 3. The Greenland error time series ranges between 10 and 130 Gt, while the Antarctica error time series ranges between 10 and 60 Gt. The magnitude is smallest over the GRACE time frame, which is expected because the stationarity assumption should inherently be close to valid during the middle years of the GRACE time frame (i.e., EOFs from limited GRACE data should still be similar to the truth EOFs). The variability in the error indicates that certain epochs are particularly sensitive to the choice of EOFs, especially around 2002 and 2014 in Greenland.

Similar results are seen even when we use only three reconstructions (instead of 30), where each of them cover gaps of similar lengths at the beginning, end, and middle part of the GRACE time frame. In other words, we believe that the estimation of this stationarity assumption error is robust. We recognize that this approach only provides a lower bound estimate: Figure 2a in *Rignot et al.* (2011) shows that the Greenland ice sheet had even larger mass balance swings before the GRACE time frame. In fact, this approach is highly limited by the SLR/DORIS fields themselves. We expect that this error estimation would be more meaningful if other independent SLR, DORIS, or SLR/DORIS fields with full covariances were available for testing.

4.3.3 Truncation Error

The need to truncate GRACE fields to match the low-resolution SLR/DORIS fields in the LSA (see Figure 1) is designated as the truncation error (red curve in Figure 3). To estimate its magnitude, we compare (1) another set of reconstructed mass change curves using simulated SLR/DORIS fields against (2) the reconstructed mass change curves using the original SLR/DORIS fields. The simulated SLR/DORIS fields are truncated GRACE fields (i.e., using only 33 Stokes coefficients instead of 3627), with covariances that belong to the original SLR/DORIS covariances. We fit these simulated low-resolution fields onto GRACE EOFs to obtain the associated PCs (as described in Section 3.3) and, ultimately, mass curves for the Greenland and Antarctic ice sheets over the GRACE time frame. Once again, inspection of the residuals (simulated minus truth) provides a sense of the errors. The resulting standard deviations of the residuals – 128 and 48 Gt for Greenland and Antarctica, respectively – indicate that truncating the fields leads to a larger error for Greenland. This is expected because the Antarctic ice sheet is a relatively isolated signals in contrast to the Greenland. In a truncated, low-resolution, long-wavelength gravity field, Greenland is influenced by its neighboring, dynamic regions (Canadian archipelago, Svalbard, Iceland, etc.). Given the lack of time-dependent bias error over the GRACE time frame, we assume that the truncation error is constant over the SLR/DORIS time frame.

4.3.4 Inherent Geophysical Errors

The reconstructed global gravity fields also contain uncertainties that are of geophysical origin and inherent to any GRACE-like data product (*Velicogna and Wahr*, 2013). We determine that the major uncertainties stem from GIA trend errors, omission of degree-1 terms, and leakage from non-tidal ocean signals (green curve in Figure 3).

Because of the long time scales associated with the viscoelastic nature of the GIA signal compared to GRACE timescales, one can represent the GIA signal as a linear one: $\mathbf{y_{GIA}} = b_{GIA}\mathbf{t}$, where we define the time vector as $\mathbf{t}$ as covering the time span of the reconstructed fields (size $N_{months} \times 1$). The error in the Greenland GIA trend is determined by taking the standard deviation of several GIA models: 4 Gt/yr from *A et al.* (2013), 1 Gt/yr from *Peltier et al.* (2015), and 20 Gt/yr from *Khan et al.* (2016). With equal weighting applied to the three models, the standard deviation is $\sigma_{b_{GIA}}^{Gre.} = 10$ Gt/yr. Similarly, for Antarctica, the various GIA trends are: 55 Gt/yr from *Ivins et al.* (2013), 69 Gt/yr from *Peltier*

et al. (2015), and 110 Gt/yr for *A et al.* (2013), yielding a standard deviation of $\sigma_{b_{GIA}}^{Ant.} = 29$ Gt/yr. However, the GIA errors are only considered when comparing trends because integrating this error from Gt/yr to Gt leads to an ambiguous choice of reference time (i.e., the integration constant).

We estimate the error due to omitting degree-1 terms (C_{10}, C_{11}, and S_{11}) from *Swenson et al.* (2008). The mass change associated to those time series adds variability with an RMS (Root-Mean-Square) over the Antarctic ice sheet of 68 Gt and over the Greenland ice sheet of 22 Gt. We assume those errors to be constant in time, but we note that these are a lower bound estimates, because the omission of degree-1 errors may lead to even larger errors prior to the GRACE period (*Ivins et al.*, 2013).

Similarly, the error due to ocean signal leaking into ice signal is estimated by computing the mass change from the GRACE GAB fields. The GAB fields are the ocean component of the Atmosphere and Ocean De-aliasing Level 1B (commonly referred to as AOD1B) background model (*Flechtner et al.*, 2015; *Dobslaw et al.*, 2013) and zero over land. We find that this signal has an RMS of 57 Gt and 32 Gt over the Antarctic and Greenland ice signal, respectively. Because the GAB fields are removed from the GRACE solutions, only GAB model errors and/or remaining non-tidal ocean signal should influence the GRACE solutions, so this approach provides an upper bound estimate of ocean signal leakage. Finally, we assume those errors are constant in time.

Velicogna and Wahr (2013) list a number of other error sources: errors in the atmosphere background models, hydrology leakage, omission of eustatic ocean, scaling associated with the kernel-averaging step (see Section 4.2). We do not consider these error sources because their magnitude are much smaller than the other errors presented here. In particular, the error on the scaling coefficient (1.3 for Greenland and 1.0 for Antarctica) originates from errors in the kernels areas (spectral vs. spatial, see Section 4.2); we estimate that these kernel areas are well constrained, so that the error on the scaling coefficient is negligible. Finally, we do not consider the errors in GRACE coefficients because they are significantly smaller than the errors in the SLR/DORIS coefficients.

4.4 Limits of the Reconstruction

We seek to address the main limits of the PCA approach: its possible inadequacy in representing non-stationary processes within the longer SLR/DORIS time frame. By applying PCA, we are trying to establish a statistical relationship between the low and high degree Stokes coefficients, while considering a shorter GRACE time series. Assume one selects n PCA derived components, which in principle represent an n-dimensional orthogonal sub-space. The orientation of this subspace is optimum in a way that the variance of the projected original GRACE signals is maximum on to the subspace. At this stage, the PCA is an optimum solution, since it does not care whether the variance is originated from a standing waveform, cyclic, or an episodic (e.g., a sudden drought, flood, or sudden earthquake) phenomenon. One should note that PCA is consciously applied here to the global domain of time-variable gravity, which means that the phenomenon of interest should be dominant enough to be reflected in the global PCA modes. The limitations of this assumption have been assessed in Section 4.3.2. We recognize,

however, that the PCA sub-space is not the best choice to represent the cyclic and episodic variations. For instance, changing the amplitude (modulation) of seasonal and interannual cycles might not be well presented by the PCA derived sub-space. The mixing of variability between PCA modes also limits achieving the best fit in the reconstruction stage. This has been to some extent reduced by removing the seasonal cycles from GRACE time series before applying the PCA. However, an application of non-stationary statistical approaches (*Forootan*, 2014) might improve the reconstruction results.

Another limitation of the reconstruction is its sensitivity to the input data. The final results are influenced by modifications in the input data in both steps of the reconstruction process: the PCA step, in which the spatial modes are defined (Section 3.1), and the LSA step, in which the temporal modes are calculated (Section 3.3). The different versions of the GRACE data (JPL, CSR, or GFZ) do not fundamentally alter the reconstruction. However, adding one of the background products (e.g., GAD) to the GSM component of the GRACE fields will yield mass change curves that differ, especially for intra-annual signals. The discrepancy at the high frequencies explains why we focus here on the shorter frequency behavior (interannual and trend behavior). Furthermore, preliminary work shows that using another set of low-degree time-variable gravity solutions has an impact on the reconstruction – neither more negative or positive than the GSFC solutions.

This study has been formulated to deliver a standard statistical reconstruction of time-variable gravity products (in the spectral domain), and to provide insights about its performance and possible errors associated with this procedure. Considering an alternative approach for improving the reconstruction is beyond the scope of this paper and will be treated in future contributions.

5 Discussion

In this section, the reconstructed global gravity fields and their errors are examined in the context of polar ice sheet mass change. We first test the validity of the reconstructed EWT maps in Greenland and Antarctica by comparing them against GRACE-only solutions over the GRACE interval. Comparing EWT maps sheds light on existing geographic differences between the reconstructions and the GRACE fields. We then compare the reconstructed mass change data against two types of data. First, two mass change curves derived only from GRACE fields are used: *Velicogna and Wahr* (2013) and *J. Wahr (personal communication)*. Second, three independent mass change data are used: Input-Output Method (IOM) data digitized from *Rignot et al.* (2011), IOM from our own data (*Enderlin et al.*, 2014; *Noël et al.*, 2015), and data from an ensemble of methods (*Shepherd et al.*, 2012). The general comparison entails a comparison of trends and a comparison of full mass change curves involving our own reconstructed vs. IOM curves.

5.1 Comparison of EWT Maps

The reconstructed EWT maps are compared to GRACE EWT maps over the GRACE interval, as shown in Figure 5. We examine the residuals, i.e., truth EWT maps minus reconstructed maps.

The means of the residuals are small for both regions: less than 0.5 cm EWT when the total change in EWT over the GRACE interval can reach 50 cm. The values of the means are negative in areas that experience high melt (south-eastern and western coast of Greenland and in West Antarctica) (*Velicogna*, 2009; *Rignot et al.*, 2011; *Shepherd et al.*, 2012), but the small values render any particular interpretation of this bias negligible. Overall, the reconstructions show no large systematic discrepancy compared to the truth fields over the GRACE interval. The residual variability reflects the reconstructions' inability to recover short-term changes and is illustrated by the standard deviation of the differences (the middle plot in Figure 5). This variability is pronounced along the south-eastern coast of Greenland and West Antarctica.

We define a customized version of Signal-to-Noise Ratio (SNR) to reflect the ability of a reconstruction to recover the truth signal as opposed to noise. We define the signal as the maximum range of change in EWT values (e.g., up to 50 cm of loss in areas of Greenland). The noise is the variability of the residuals (the middle column in Figure 5), since the means of the residuals are negligible. This SNR measure is skewed towards large values in pixels where the trends are large, but appropriately highlights the areas where the variability in the residuals is large compared to the signal. Such areas are the north-east coast of Greenland and the interior of Antarctica, where the trend in mass loss is relatively small (*Velicogna*, 2009; *Rignot et al.*, 2011; *Shepherd et al.*, 2012). Overall, the fact that areas of high mass loss contain high SNR values gives us confidence that the reconstructions capture meaningful signal during the GRACE time frame.

5.2 Greenland Mass Change

Figure 6 shows the different mass change curves for the Greenland ice sheet.

First, we focus on the reconstruction, represented as the blue curve in Figure 6. With the perspective of an additional decade of data, best-fit trends applied to our reconstructed mass change curve suggests two distinct epochs of approximately linear mass loss prior to and following 2005. From 1993 to 2005, the mass change trend is -70±20 Gt/yr, while the next decade shows a trend of -360±28 Gt/yr. The trend errors are the formal errors of the linear regression.

The transition to a faster rate of mass loss around 2005 is concurrent with an increase in mass loss due to surface meltwater runoff (*van Angelen et al.*, 2014; *Enderlin et al.*, 2014). Independent polar motion data also indicate that rapid ice mass loss is the cause of the observed change in the direction of the mean pole of the Earth (*Chen et al.*, 2013; *Wahr et al.*, 2015). Figure 2 in *Chen et al.* (2013) shows the deviation of the annual mean pole from the long-term trend starting in 2005 using IERS pole motion data. *Wahr et al.* (2015) also discuss this deviation from a long-term (20th century) trend of the mean pole (see Figure 1) and its impact on GRACE C_{21} and S_{21}. On the other hand, we recognize that the mass change of the Greenland ice sheet is influenced by many factors, such as circulation in the North Atlantic (*Seo et al.*, 2015), and that our current interpretation is limited in its scope.

A comparison between the reconstruction and the GRACE-only solution (red curve in Figure 6) shows that the reconstruction has higher artificial variability, but overall the GRACE-only curve is within the 1-σ envelope.

Furthermore, we compare the reconstructed mass curve before the GRACE time frame. Despite the lack of independent time-variable gravity data, we generate mass change curves extending back to 1992 from two other approaches. First, we compute our own IOM curve, shown in black in Figure 6. The IOM obtains mass change estimates by subtracting yearly ice discharge across the grounding line (*Enderlin et al.*, 2014) from monthly surface mass balance (SMB) determined from the RACMO2.3 atmospheric model (*Noël et al.*, 2015; *van den Broeke et al.*, 2016). We divide the yearly ice discharge data by 12 to obtain monthly discharge values. One drawback of this simple conversion is that seasonal variations are neglected, but this is acceptable because this study is focused on interannual signals. Furthermore, seasonal changes in the velocity of Greenland's fast-flowing marine-terminating glaciers, and presumably ice discharge as well, are relatively small *Moon et al.* (2014). The SMB data are also filtered in order to remove their seasonal signals, both the annual and semi-annual components. Furthermore, the ice discharge data only start in 2000 and are extrapolated to 1992 using two assumptions: (1) a linear trend from 1996 to 2000 and (2) ice discharge changes of zero from 1992 to 1996, which are common assumptions for the computation of mass loss estimates due to discharge change (*van den Broeke et al.*, 2016; *Enderlin et al.*, 2014). Second, we digitize mass balance data from Figure 2a in *Rignot et al.* (2011) and plot the integrated values, as seen by the green line in Figure 6.

Generally speaking, the three curves match well to each other and all indicate an increase in mass change rate since the early 1990s, even though the reconstruction show larger mass change before 2000. The biggest difference is in the rapid mass loss in 1998 followed by a multi-year mass gain. This dip is clearly not observed in the other curves and remains unexplainable. We associate such dip (along with smaller variability in 1996, 1997, 2002, and 2003) with the limits of the SLR/DORIS solution that have not been accounted for in the error budget. This highlights the need for independent conventional tracking data to account for the unknown errors in the SLR/DORIS fields that influence the reconstructions, but are not captured in the covariances.

Comparisons of mass change trends from this study and previous analyses are presented in Table 2. The *Rignot et al.* (2011) data are not included in this table because the detailed and full time series required for a rigorous fit are unavailable. The comparisons are applied to matching time intervals. We notice that Greenland trends for this study's reconstruction are consistently higher than previous analyses by 15-25%. One potential reason for this consistent bias is signal leakage from surrounding melting regions (Baffin island, Ellesmere island, and Iceland) that is absorbed by temporal mode 1 during the process of fitting SLR/DORIS coefficients onto spatial modes, due to resolution difference in the fitting. An earlier study estimates the mass loss in these regions to be 51 ± 17 Gt/yr (*Schrama and Wouters*, 2011) and 42 ± 24 Gt/yr (*Rignot et al.*, 2011). Furthermore, differences in processing (e.g., the recently recommended corrections for C_{21} and S_{21} outlined in (*Wahr et al.*, 2015), which influence the reconstructed Greenland trend by about -10 Gt/yr, but not Antarctica) also likely lead to discrepancies in estimates of mass loss between the different datasets in Table 2. Hence, these two sources of extra loss in mass change could perhaps explain the differences with the other studies. Finally, the trends calculated using the earliest time frame available (1993 – 2000) show higher mass loss by 102 and 78 Gt/yr for our reconstruction as compared to the IOM and the ensemble solution in *Shepherd et al.* (2012), respectively.

Although the mass loss acceleration fit reported in previous studies could also provide a useful metric for our comparisons, we refrain from using such fits as a means for comparison because the acceleration estimates are highly sensitive to the time frames selected (*Wouters et al.*, 2013). For reference, however, we estimate that the acceleration of the full reconstructed Greenland mass change time series is -24$\pm$6 Gt/yr^2. This value represents the quadratic coefficient a, where $M(t) \approx \frac{1}{2}at^2 + bt + c$.

In summary, we find that the magnitude of the Greenland ice sheet balance appears to have increased approximately five-fold after 2005. Despite the lack of independent time-variable gravity data, we compare our reconstruction to two separate IOM approaches. The reconstruction shows higher mass loss before 2000 and presents variability, in particular a large dip in the late 1990s, that is not visible in the IOM curves. However, our comparisons are hindered by a number of assumptions (such as assuming linear mass loss before 2000 and zero changes before 1996 for the extrapolated *Enderlin et al.* (2014) ice discharge) and the fact that data are digitized (Figure 2 in *Rignot et al.* (2011)). The comparison of trends over different time intervals shows that the reconstruction has a higher mass loss rate of between 39-53 Gt/yr over the GRACE interval. Even when taking into account this additional rate, the mass loss from the reconstructions are still higher than the other methods before 1993, suggesting higher mass loss than previously thought in the 1990s.

5.3 Antarctica Mass Change

Figure 7 shows the different mass change curves for the Antarctic ice sheet.

Unlike the Greenland ice sheet, the behavior of the Antarctic ice sheet as a whole is heavily influenced by interannual variations and counter-balancing regional effects (*van de Berg et al.*, 2006). Although previous analyses found acceleration of mass loss for the entire Antarctic ice sheet (*Velicogna*, 2009; *Rignot et al.*, 2011; *Shepherd et al.*, 2012), our reconstructed mass change suggests three distinct mass change regimes since 1993. Before 2000, the ice sheet lost mass at a rate of -56$\pm$28 Gt/yr before being in mass balance from approximately 2000 to 2005 as the ice sheet balance was 20$\pm$41 Gt/yr. After 2005, the ice sheet lost mass at almost twice the rate of the earlier mass loss rate of -103$\pm$20 Gt/yr. The error on the trend values are large, highlighting the uncertainties that stem from GIA trend errors (see Section 4.3.4).

The GRACE-only mass curve, represented as the red curve in Figure 7, is in excellent agreement with the reconstruction and well within its error envelope. We also compare the reconstruction against an IOM curve. The first IOM approach applied in Greenland that used ice discharge data and surface mass balance from atmospheric models (black curve in Figure 6) was not reproduced because the *Enderlin et al.* (2014) analysis was restricted to Greenland. We were still able to digitize Figure 2b from *Rignot et al.* (2011) to provide perspective prior to 2003. The large trend difference between the two curves is prohibitively large and remains unexplained. Potential explanations for this discrepancy will be explored as part of future work. On one hand, source of uncertainty in IOM include uncertainty in the SMB and uncertainty in discharge caused by bed elevation uncertainty (which can be on the order of tens to hundreds of meters) and/or location of the

grounding line (which can influence discharge estimates) (*Enderlin et al.*, 2014). On the other hand, refinements of GIA models will continue to influence the trend of GRACE-based estimates.

The ensemble study from *Shepherd et al.* (2012) shows similar trend numbers to the reconstructions, even before 2003, despite the large error bars. Over the GRACE time frame, the comparisons of trends against other gravimetric analyses that use similar GIA models show strong agreement, as seen Table 2.

6 Summary

In this study, we reconstruct global, time-variable gravity fields by combining GRACE fields with low-resolution fields from SLR/DORIS tracking data that start in November 1992. We generate basis functions from a PCA on the GRACE fields and project the truncated version of the basis functions onto SLR/DORIS fields to find their temporal behavior. We reconstruct the global gravity fields by combining these temporal amplitudes with the full basis functions. Smoothed mass change curves over Greenland and Antarctica spanning April 1993 to November 2013 are generated from these reconstructed fields. The additional decade prior to the GRACE period allows for further interpretation of their mass change behavior in time. The current time frame of the reconstructions are limited by the SLR/DORIS data, which for now only extend until April 2014. An error budget is assessed and quantifies uncertainties that arise from the assumptions made in the reconstruction process (stationary GRACE modes, truncated modes used in the LSA) as well as uncertainties that are inherent to global gravity fields.

The mass change of the Greenland ice sheet can be described by two periods of linear mass loss with the rate of mass loss about five times larger after 2005 than over the 1993 – 2005 time frame. The Antarctic ice sheet appears to have experienced no noticeable mass change in the early 2000s, while experiencing a mass loss rate prior to 2000 that is less than half of the mass loss rate of the late 2000s. However, the validation of the mass change curves is limited by the lack of glaciological data in the 1990s. Moreover, a comparison over the GRACE time frame shows robust agreement for Antarctica and some discrepancies for Greenland, which shows extraneous variability.

Finally, by combining GRACE and SLR/DORIS over overlapping periods, the PCA method augments the capability of gravity fields derived without GRACE, including over potential gaps between GRACE and its successor mission GRACE Follow-On. Preliminary work with simulations of gaps in GRACE-like data show that the long-term behavior of reconstructions will not be influenced by one to two year gaps. Furthermore, the influence of the low-resolution fields (here, the SLR/DORIS solutions from GSFC) on the final reconstructions will be further assessed when other SLR solutions and their full covariances are available. Overall, the reconstructed time series of Greenland and Antarctic ice sheet mass change provide a new perspective on the balance of polar ice sheets by combining satellite gravity products starting in the early 1990s.

References

A, G., J. Wahr, and S. Zhong (2013), Computations of the viscoelastic response of a 3-D compressible Earth to surface loading: an application to Glacial Isostatic Adjustment in Antarctica and Canada, *Geophys. J. Int.*, *192*(doi:10.1093/gji/ggs030), 557–572.

Baur, O. (2013), Greenland mass variation from time-variable gravity in the absence of GRACE, *Geophys. Res. Lett.*, *40*, 4289–4293, doi:10.1002/grl.50881.

Bettadpur, S. (2012), *UTCSR Level-2 processing standards document (For Level-2 Product Release 0005)*, Center for Space Research, The University of Texas at Austin, Austin, TX.

Cerri, L., J. M. Lemoine, F. Mercier, N. P. Zelensky, and F. G. R. Lemoine (2013), DORIS-based point mascons for the long term stability of precise orbit solutions, *Adv. Space. Res.*, *52*, 466–476, doi:10.1016/j.asr.2013.03.023.

Chen, J. L., C. R. Wilson, J. C. Ries, and B. D. Tapley (2013), Rapid ice melting drives Earth's pole to the East, *Geophys. Res. Lett.*, *40*, 2625–2630, doi:10.1002/grl.50552.

Cheng, M., J. C. Ries, and B. D. Tapley (2011), Variations of the Earth's figure axis from satellite laser ranging and GRACE, *J. Geophys. Res.*, *116*, B01,409, doi:10.1029/2010JB000850.

Cheng, M., B. D. Tapley, and J. C. Ries (2013), Deceleration in the Earth's oblateness, *J. Geophys. Res.-Sol. Ea.*, *118*, 740–747, doi:10.1002/jgrb.50058.

Church, J. A., and N. J. White (2002), A 20th century acceleration in global sea-level rise, *Geophys. Res. Lett.*, *33*, L01,602, doi:10.1029/2005GL024826.

Cox, C. M., and B. F. Chao (2002), Detection of a Large-Scale Mass Redistribution in the Terrestrial System since 1998, *Science*, *297*, 831, doi:10.1126/science.1072188.

Dahle, C., F. Flechtner, C. Gruber, D. König, R. König, G. Michalak, and K. H. Neumayer (2013), *GFZ GRACE Level-2 processing standards document for level-2 product release 0005*, Helmholtz-Zentrum Potsdam, Deutsches GeoForschungsZentrum, Potsdam, Germany., Scientific Technical Report STR12/02 ed.

Dobslaw, H., F. Flechtner, I. Bergmann-Wolf, C. Dahle, R. Dill, S. Esselbom, I. Sagsen, and M. Thomas (2013), Simulating high-frequency atmosphere-ocean mass variability for dealiasing of satellite gravity observations: AOD1 RL05, *J. Geophys. Res. Oceans*, *118*, 3704–3711.

Enderlin, E. M., I. M. Howat, S. Jeong, M.-J. Noh, J. H. van Angelen, and M. R. van den Broeke (2014), An improved mass budget for the Greenland ice sheet, *Geophys. Res. Lett.*, *41*, 866–872, doi:10.1002/2013GL059010.

Flechtner, F., H. Dobslaw, and E. Fagiolini (2015), *AOD1B Product Description Document for Product Release 05*, GFZ German Research Centre for Geosciences.

Forootan, E. (2014), Statistical signal decomposition techniques for analyzing time-variable satellite gravimetry data, Ph.D. thesis, Universität Bonn, http://hss.ulb.uni-bonn.de/2014/3766/3766.htm.

Forootan, E., and J. Kusche (2012), Separation of global time-variable gravity signals into maximally independent components, *J. Geod.*, *86*, 477–497, doi: 10.1007/s00190-011-0532-5.

Haberkorn, C., M. Bloßfeld, J. Bouman, M. Fuchs, and M. Schmidt (2015), Towards a consistent estimation of the earth's gravity field by combining normal equation matrices from grace and slr, *IAG Symp Ser*, pp. 1–7.

Hamlington, B. D., R. R. Leben, R. S. Nerem, W. Han, and K.-Y. Kim (2011), Reconstructing sea level using cyclostationary empirical orthogonal functions, *J. Geophys. Res.*, *116*, C12,015, doi:10.1029/2011JC007529.

Ivins, E. R., T. S. James, J. Wahr, E. J. O. Schrama, F. W. Landerer, and K. M. Simon (2013), Antarctic contribution to sea level rise observed by GRACE with improved GIA correction, *J. Geophys. Res.-Sol. Ea.*, *118*(doi:10.1002/jgrb.50208), 3126–3141.

James, T. S., and E. R. Ivins (1997), Global geodetic signatures of the Antarctic ice sheet, *J. Geophys. Res.*, *102*, 605–633.

Jekeli, C. (1981), *Alternative Methods to Smooth the Earth's Gravity Field*, Geodetic and GeoInformation Science, Department of Civil and Environmental Engineering and Geodetic Science, The Ohio State University.

Kaplan, A., Y. Kushnir, and M. A. Cane (2000), Reduced Space Optimal Interpolation of Historical Marine Sea Level Pressure: 1854-1992, *Bull. Amer. Meteor. Soc.*, *13*, 2987–3002.

Khan, S. A., et al. (2016), Geodetic measurements reveal similarities between post-Last Glacial Maximum and present-day mass loss from the Greenland ice sheet, *Sci. Adv.*, *2*(doi:10.1126/sciadv.1600931).

Koch, K. R. (1988), *Parameter estimation and hypothesis testing in linear models*, Springer, New York. ISBN:9783540652571.

Lemoine, F. G., et al. (2010), Towards development of a consistent orbit series for TOPEX, Jason-1, and Jason-2, *Adv. Space Res.*, *46*, 1513–1540.

Lemoine, F. G., D. S. Chinn, N. P. Zelensky, and J. W. Beall (2014), Time-Variable Gravity Solutions from 1993-2014 from SLR and DORIS data, Abstract G23A-0472, in *American Geophysical Union Fall Meeting, San Francisco, California, 15-19, 2014*.

Lemoine, F. G., D. S. Chinn, N. P. Zelensky, J. W. Beall, and K. L. Bail (2016), The development of the gsfc doris contribution to itrf2014, *Adv. Space. Res., in press*, doi:10.106/j.asr.2015.12.043.

Longuevergne, L., B. R. Scanlon, and C. R. Wilson (2010), GRACE Hydrological estimates for small basins: Evaluating processing approaches on the High Plains Aquifer, USA, *Water Resour. Res.*, *46*(W11517).

Matsuo, K., B. F. Chao, T. Otsubo, and K. Heki (2013), Accelerated ice mass depletion revealed by low-degree gravity field from satellite laser ranging: Greenland, 1991-2011, *Geophys. Res. Lett.*, *40*, doi:10.1002/grl.50900.

Moon, T., I. Joughin, B. Smith, M. R. V. den Broeke, W. J. V. de Berg, B. Noël, and M. Usher (2014), Distinct patterns of seasonal Greenland glacier velocity, *Geophys. Res. Lett.*, *41*(doi:10.1002/2014GL061836), 7209–7216.

Morrow, E., J. X. Mitrovica, M. G. Sterenborg, and C. Harig (2013), A test of recent inferences of net polar ice mass balance based on long-wavelength gravity,

Bull. Amer. Meteor. Soc., *26*, 6535–6540, doi:10.1175/JCLI-D-13-00078.1.

Nerem, R. S., and J. Wahr (2011), Recent changes in the Earth's oblateness driven by Greenland and Antarctic ice mass loss, *Geophys. Res. Lett.*, *38*, L13,501, doi: 10.1029/2011GL047879.

Noël, B., W. J. van de Berg, E. van Meijgaard, P. K. Munneke, R. S. W. van de Wal, and M. R. van den Broeke (2015), Evaluation of the updated regional climate model RACMO2.3: summer snowfall impact on the Greenland Ice Sheet, *The Cryosphere*, *9*, 1831–1844, doi:10.5194/tcd-9-1831-2015.

North, G. R., T. L. Bell, R. F. Cahalan, and F. J. Moeng (1982), Sampling errors in the estimation of Empirical Orthogonal Functions, *Bull. Amer. Meteor. Soc.*, *110*, 699–710.

Peltier, W. R., D. F. Argus, and R. Drummond (2015), Space geodesy constrains ice age terminal glaciation: The global ICE-6G_C (VM5a) model, *J. Geophys. Res.-Sol. Ea.*, *120*, 450–487, doi:10.1002/2014JB011176.

Preisendorfer, R. (1988), *Principal component analysis in meteorology and oceanography*, Elsevier, Amsterdam. ISBN:0444430148.

Ray, R. D., and B. C. Douglas (2011), Experiments in reconstructing twentieth-century sea levels, *Prog. Oceanogr.*, *91*, 496–515, doi:10.1016/j.pocean.2011.07.021.

Rignot, E., I. Velicogna, M. van den Broeke, A. Monaghan, and J. T. M. Lenaerts (2011), Acceleration of the contribution of the Greenland and Antarctic ice sheets to sea level rise, *Geophys. Res. Lett.*, *38*, L05,503, doi:10.1029/2011GL046583.

Rodell, M., et al. (2004), The Global Land Data Assimilation System, *Bull. Amer. Meteor. Soc.*, *85*(3), 381–394.

Schrama, E. J. O., and B. Wouters (2011), Revisiting Greenland ice sheet mass loss observed by GRACE, *J. Geophys. Res.*, *116*, B02,407, doi:10.1029/2009JB006847.

Seo, K.-W., D. E. Waliser, C.-K. Lee, B. Tian, T. Scambos, B.-M. Kim, J. H. van Angelen, and M. R. van den Broeke (2015), Accelerated mass loss from Greenland ice sheet: Links to atmospheric circulation in the North Atlantic, *Global Planet. Change*, *128*, 61–71.

Shepherd, A., et al. (2012), A Reconciled Estimate of Ice-Sheet Mass Balance, *Science*, *338*, 1183, doi:10.1126/science.1228102.

Sośnica, K., A. Jäggi, U. Meyer, D. Thaller, G. Beutler, D. Arnold, and R. Dach (2015), Time variable Earth's gravity field from SLR satellites, *J. Geod.*, *89*(10), 945–960, doi:10.1007/s00190-015-0825-1.

Swenson, S., and J. Wahr (2002), Methods for inferring regional surface-mass anomalies from Gravity Recovery And Climate Experiment (GRACE) measurements of time-variable gravity, *J. Geophys. Res.*, *107*(B9), 2193, doi:10.1029/2001JB000576.

Swenson, S., and J. Wahr (2006), Post-processing removal of correlated errors in GRACE data, *Geophys. Res. Lett.*, *33*, L08,402, doi:10.1029/2005GL025285.

Swenson, S., D. Chambers, and J. Wahr (2008), Estimating geocenter variations from a combination of GRACE and ocean model output, *J. Geophys. Res.*, *113*(doi:10.1029/2007JB005338), B08,410.

Tapley, B. D., S. Bettadpur, M. Watkins, and C. Reigber (2004), The gravity recovery and climate experiment: Mission overview and early results, *Geophys. Res. Lett.*, *31*, L09,607, doi:10.1029/2004GL019920.

Tosi, N., R. Sabadini, and A. M. Marotta (2005), Simultaneous inversion for the Earth's mantle viscosity and ice mass imbalance in Antarctic and Greenland, *J. Geophys. Res.*, *110* (doi:10.1029/2004JB003236), B07,402.

van Angelen, J. H., M. R. van den Broeke, B. Wouters, and J. T. M. Lenaerts (2014), Contemporary (1960-2012) Evolution of the Climate and Surface Mass Balance of the Greenland Ice Sheet, *Surv. Geophys.*, *35*, 1155–1174, doi:10.1007/s10712-013-9261-z.

van de Berg, W. J., M. R. van den Broeke, C. H. Reijmer, and E. van Meijgaard (2006), Reassessment of the Antarctic surface mass balance using calibrated output of a regional atmospheric climate model, *J. Geophys. Res.*, *111*, D11,104, doi:10.1029/2005JD006495.

van den Broeke, M. R., E. M. Enderlin, I. M. Howat, P. K. Munneke, B. Y. P. Noël, W. J. van de Berg, E. van Meijgaard, and B. Wouters (2016), On the recent contribution of the Greenland ice sheet to sea level change, *The Cryosphere*, *10* (DOI:10.5194/tc-10-1933-2016), 1933–1946.

Velicogna, I. (2009), Increasing rates of ice mass loss from the Greenland and Antarctic ice sheets revealed by GRACE, *Geophys. Res. Lett.*, *36*, L19,503, doi:10.1029/2009GL040222.

Velicogna, I., and J. Wahr (2006), Measurements of Time-Variable Gravity Show Mass Loss in Antarctica, *Science*, *311*, 1754–1756, doi:10.1126/science.1123785.

Velicogna, I., and J. Wahr (2013), Time-variable gravity observations of ice sheet mass balance: Precision and limitations of the GRACE satellite data, *Geophys. Res. Lett.*, *40*, 3055–3063, doi:10.1002/grl.50527.

Wahr, J., M. Molenaar, and F. Bryan (1998), Time variability of the Earth's gravity field: Hydrological and oceanic effects and their possible detection using GRACE, *J. Geophys. Res.*, *103* (B12), 30,205–30,229, doi:10.1029/98JB02844.

Wahr, J., R. S. Nerem, and S. Bettadpur (2015), The pole tide and its effect on GRACE time-variable gravity measurements: Implications for estimates of surface mass variations, *J. Geophys. Res.-Sol. Ea.*, *120* (6), 4597–4615, doi:10.1002/2015JB011986.

Watkins, M. M., and D.-N. Yuan (2014), *JPL Level-2 Processing Standards Document*, Jet Propulsion Laboratory, California Institute of Technology, Pasadena, CA.

Weigelt, M., T. van Dam, A. Jäggi, L. Prange, M. J. Tourian, W. Keller, and N. Sneeuw (2013), Time-varity gravity signal in Greenland revealed by high-low satellite-to-satellite tracking, *J. Geophys. Res.*, *118*, 3848–3859, doi:10.1002/jgrb.50283.

Whitehouse, P. L., M. J. Bentley, G. A. Milne, M. A. King, and I. D. Thomas (2012), A new glacial isostatic adjustment model for Antarctica: calibrated and tested using observations of relative sea-level change and present-day uplift rates, *Geophys. J. Int.*, *180*, 1464–1482.

Wouters, B., J. L. Bamber, M. R. van den Broeke, J. T. M. Lenaerts, and I. Sasgen (2013), Limits in detecting acceleration of ice sheet mass loss to climate variability, *Nat. Geosci.*, *6*, doi:10.1038/NGEO1874.

Zehentner, N., and T. Mayer-Gürr (2015), SST-hl: Time variable gravity from multiple non-dedicated satellites, in *EGU General Assembly Conference Abstracts*, *EGU General Assembly Conference Abstracts*, vol. 17, p. 10613.
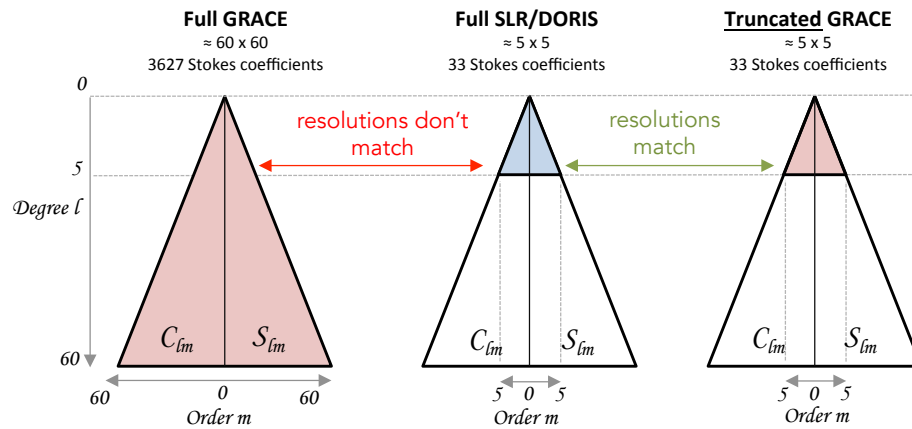
Fig. 1 Schematic of the truncation of GRACE fields to match the resolution of SLR/DORIS fields. The triangle shape illustrates the underlying data of gravity fields: Stokes coefficients (*Wahr et al.*, 1998). Low degrees (l) have few orders ($m = [0, ..., l]$) and are at the top of the triangle, while high degrees have many more orders and are at the bottom. GRACE fields have 3627 coefficients while the SLR/DORIS only have 33. As such, the Least Squares Adjustment of SLR/DORIS coefficients on GRACE EOFs (Section 3.3) requires that GRACE EOFs are truncated to similar resolution and that higher degree coefficients be removed.
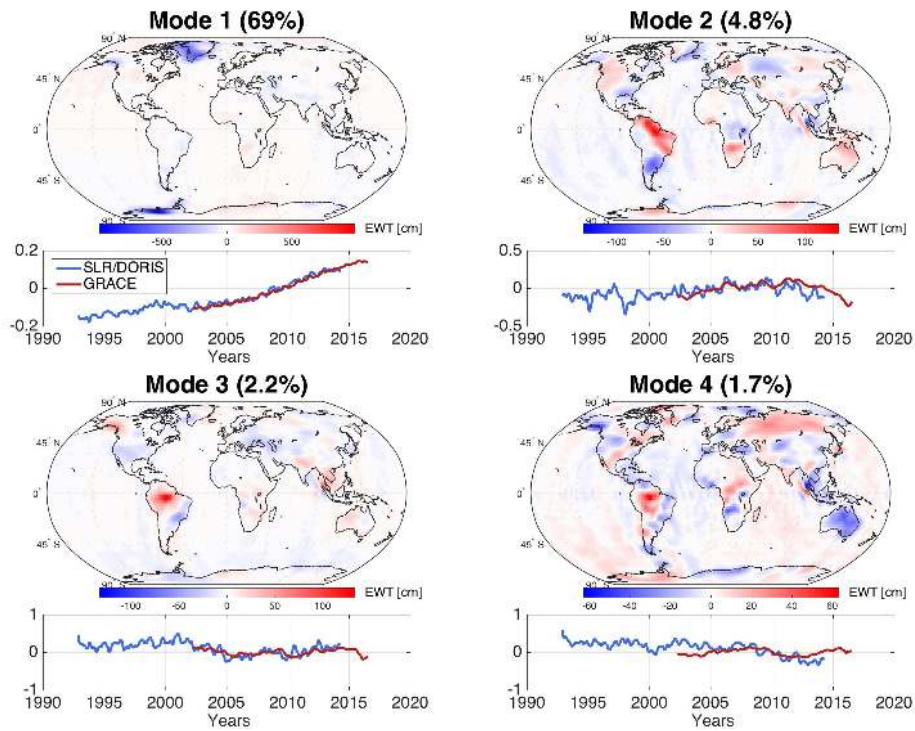
Fig. 2 The four dominant spatial and temporal patterns from GRACE and SLR/DORIS time-variable gravity data. The global spatial modes (EOFs) from the PCA decomposition of GRACE fields and the percent of variance captured are shown. Right below each global map are their associated normalized temporal modes (PCs) directly from a GRACE PCA (red curve) and from SLR/DORIS (blue curve, see Section 3.3).
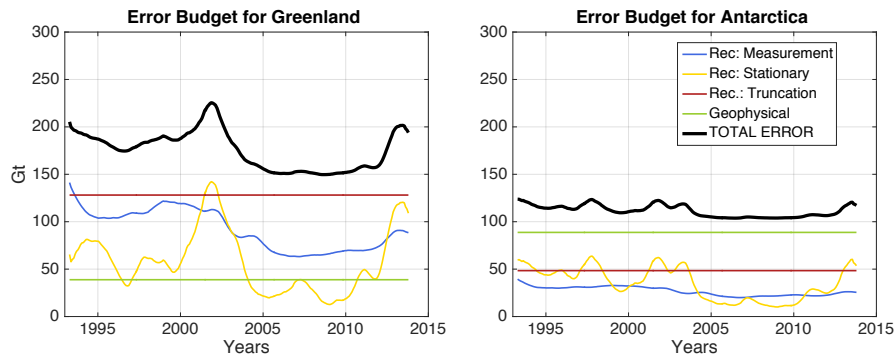
Fig. 3 Error budget for the Greenland and Antarctic ice sheet mass change reconstruction in Gt. The blue curve denotes the measurement error (Section 4.3.1), the yellow curve the stationarity assumption error (Section 4.3.2), the red curve the truncation error (Section 4.3.3), and the green curve the geophysical error (Section 4.3.4). The total error budget is obtained by adding all the errors in quadrature and denoted as the thicker black curve.
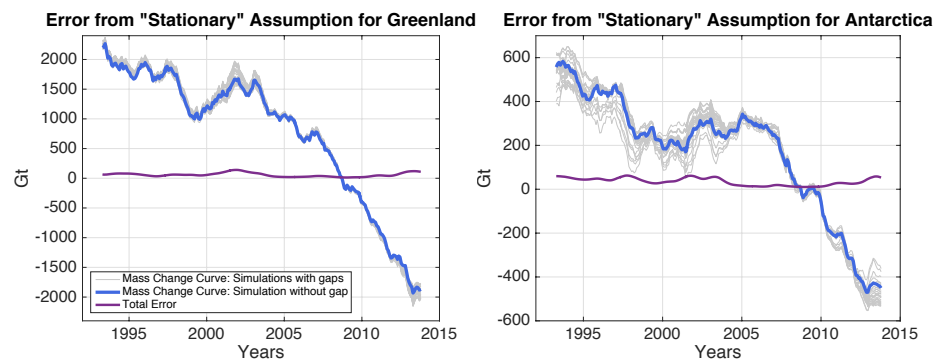

Fig. 4 Assessing the stationarity assumption error (see Section 4.3.2). The blue curve denotes the reconstruction using the full set of available GRACE data, whereas the 30 gray lines denote the simulated reconstructions that have simulated "pseudo-randomly"-generated gaps in the GRACE data. The mean of the residuals (simulated minus truth) is shown in purple and represents the stationarity assumption error. It is worth noting that the simulated reconstructions for Greenland are very similar to the reconstruction that used the full set of GRACE data.
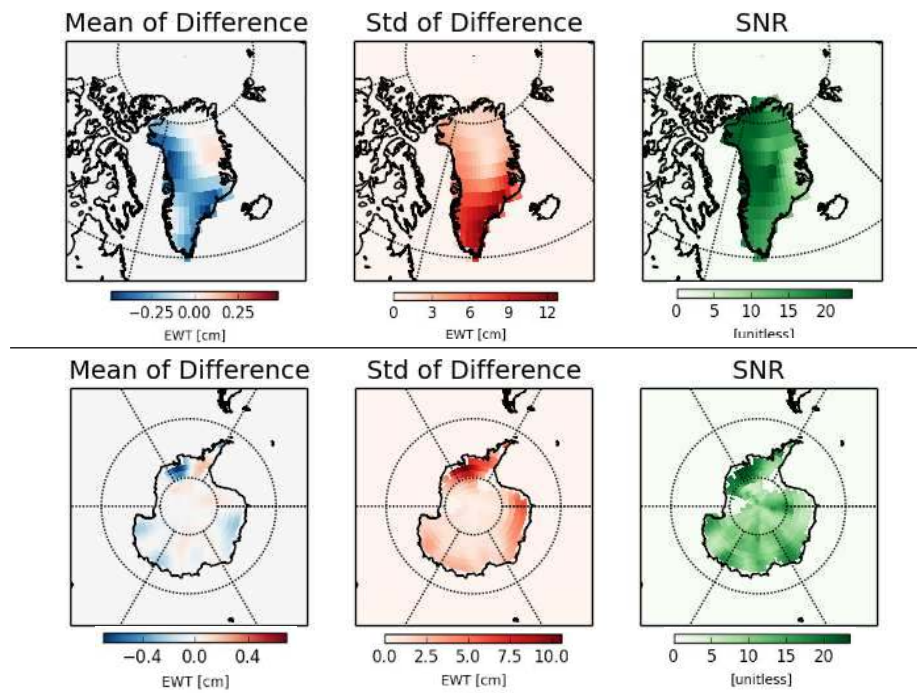
Fig. 5 Quality of reconstructed gravity fields in Greenland (top row) and Antarctica (bottom row). The first two columns show the mean and the standard deviation of the difference between truth EWT maps (GRACE-only) and PCA reconstructions over the GRACE interval. The last column shows the signal-to-noise ratio.
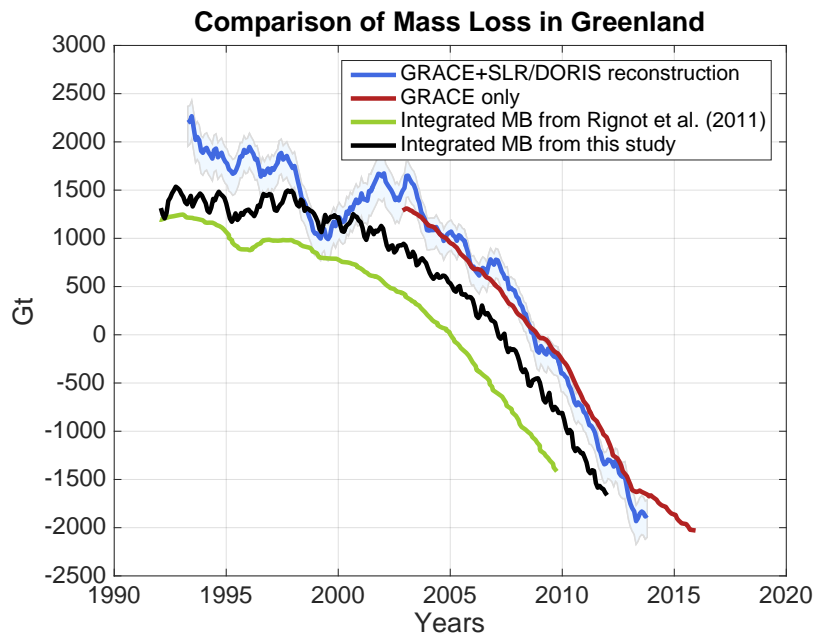
Fig. 6 Change in Greenland ice sheet mass in Gt. The red curve denotes the mass change from GRACE and the blue curve denotes the mass change from the reconstruction (GRACE+SLR/DORIS). The light blue area shows the 1-σ uncertainty envelope. The green curve shows the integrated mass balance obtained from digitizing Figure 2a in *Rignot et al.* (2011) and the black curve the integrated mass balance obtained from this study. This study's mass balance used surface mass balance from *Noël et al.* (2015) and the ice discharge from *Enderlin et al.* (2014). The black and green curves are each shifted by 400 and 800 Gt to provide a less cluttered view.
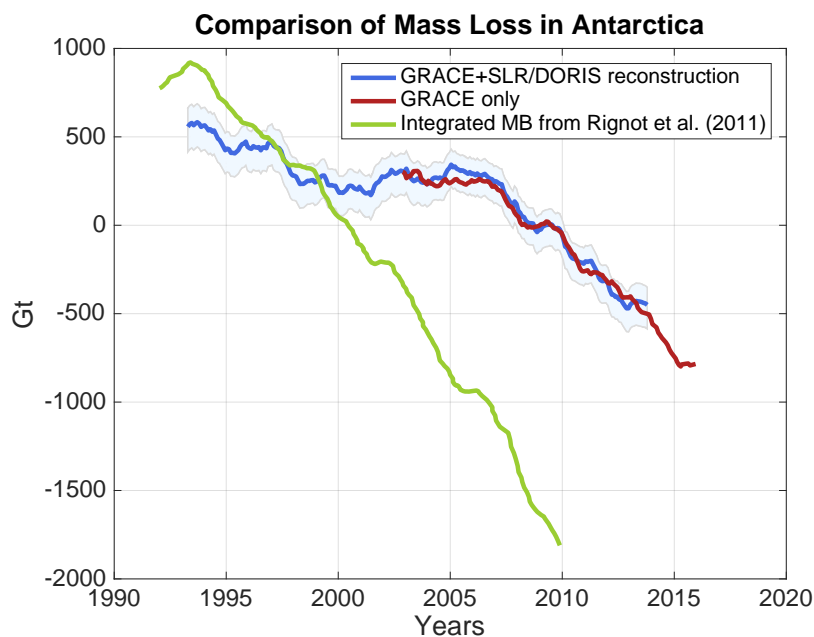
Fig. 7 Change in Antarctic ice sheet mass in Gt. The red curve denotes the mass change from GRACE and the blue curve denotes the mass change from the reconstruction (GRACE+SLR/DORIS). The light blue area shows the 1-σ uncertainty envelope. The green curve shows the integrated mass balance obtained from digitizing Figure 2b in *Rignot et al.* (2011).

Table 1 The two types of satellite-derived, global gravity datasets merged.

Name	**SLR** (Satellite Laser Ranging) / **DORIS** (Doppler Orbitography and Radiopositioning Integrated by Satellite)	**GRACE** (Gravity Recovery And Climate Experiment)
Processing center	Goddard Space Flight Center (GSFC) (*Lemoine et al.*, 2014)	Center for Space Research (CSR) at UT-Austin (*Bettadpur*, 2012)
Orbital configuration	7-18 satellites in a variety of orbits and altitudes	Twin-satellite in polar orbit, 450 km altitude
Tracking	Ground-based tracking: laser ranging and Doppler	Satellite-to-satellite in low-low mode
Harmonics	33 Stokes coefficients (incomplete degree and order 5×5): without C_{50} and with C_{61} and S_{61}	3627 Stokes coefficients (degree and order 60×52), where the last eight orders are removed in the destriping algorithm (*Swenson and Wahr*, 2006)
Resolution	$\approx 3{,}300 - 4{,}000$ km	≈ 330 km
Timespan	November 1992 – April 2014	April 2002 – June 2016

Table 2 Comparison of trend values for the Greenland and Antarctic ice sheet mass change curves over several time frames. The trend fit values are calculated from a least squares adjustment of the time series. The 1-σ trend errors are the formal errors obtained from the covariance matrix of the linear regression. For each ice sheet, we show the trend value from a study cited in the left column and the equivalent trend value from the reconstructed mass change curves in the column titled "G+SD" (meaning GRACE+SLR/DORIS). *Velicogna and Wahr* (2013) use GRACE RL05 gravimetry solutions and a combination of the global ICE-5G GIA model and the regional IJ05_R2 GIA model (*Ivins et al.*, 2013); [*J. Wahr, personal communication*] also uses GRACE CSR RL05 and ICE-6G (*Peltier et al.*, 2015); *Shepherd et al.* (2012) use an ensemble of methods (gravimetry, altimetry, etc.) and a combination of W12a (*Whitehouse et al.*, 2012) and IJ05_R2 (*Ivins et al.*, 2013) as GIA models. See Section 5.2 for a description of the Input-Output Method results computed in this study.

Name	Timespan	Greenland Trend [Gt/yr]		Antarctica Trend [Gt/yr]	
		Study	Talpe et al. (G+SD)	Study	Talpe et al. (G+SD)
Velicogna et al. (2013)	01/2003 − 11/2012	-258 ± 41	-311 ± 24	-83 ± 49	-80 ± 32
Shepherd et al. (2012)	06/2005 − 12/2010	-263 ± 30	-311 ± 50	-87 ± 43	-98 ± 46
	01/1993 − 12/2011	-142 ± 49	-130 ± 22	-71 ± 53	-30 ± 33
	01/1993 − 12/2000	-51 ± 65	-129 ± 35	-48 ± 65	-54 ± 36
Wahr, John (pers. comm.)	10/2002 − 11/2013	-275 ± 9	-321 ± 22	-78 ± 29	-80 ± 31
Input-Output Method	01/1993 − 12/2011	-136 ± 11	-129 ± 26	-	-
	01/1993 − 12/2000	-27 ± 11	-129 ± 39	-	-
Talpe et al. (GRACE only)	10/2002 − 12/2013	-282 ± 29	-321 ± 22	-76 ± 29	-80 ± 31